# Monitoring DNA double strand break repair in *Saccharomyces cerevisiae* at high throughput and high resolution

**Yael Shalev Ezra[1], Alon Saguy[1], Gaia Levin[1], Lucien E. Weiss[2], Onit Alalouf[1], Yoav Shechtman[1,3*].**

[1] Department of Biomedical Engineering, Technion – Israel Institute of Technology, Haifa, 3200003, Israel

[2] Department of Engineering Physics, Polytechnique Montréal, Montreal, QC, H3T 1J4, Canada

[3] Department of Mechanical Engineering, University of Texas at Austin, TX, USA

* To whom correspondence should be addressed. Tel: +972-778871422; Fax: +972-778871423; Email: yoavsh@technion.ac.il

**KEYWORDS**

Mating type switching, Double-strand break repair, PSF engineering, Image flow cytometry, DNA dynamics.

**ABSTRACT**

The yeast mating type switching process is used as a biological model system to study eukaryotic DNA double strand break (DSB) repair, a process of fundamental importance in health and disease. However, tools for tracking the mating type switching process in real-time in live cells are limited. We developed methods to follow and quantify mating type switching occurrence in real-time, at the single live cell level, applicable for detection of rare events and population heterogeneity. First, we show, using a fluorescent reporter in live cells, that switching probability in strains tagged by a fluorescent repressor-operator system (FROS) is reduced, not only due to the integration of operator repeats, but also due to the overexpressed fluorescent molecules in the nucleus. Next, by applying wavefront shaping to imaging flow cytometry, we collected 3D data in high throughput, and were able to differentiate between MATa and MATα conformation and to detect DNA dynamics during switching with unprecedented spatial and temporal resolutions. Using a strain with the *MAT-stk* mutation, which gives rise to inefficient HO endonuclease DSB activity, we discriminated between two consecutive distances between the HMLα and the MAT loci upon DNA damage. We suggest

that initial nearing between the loci occurs for both single and double strand breaks, and further and closer proximity occurs for DSB only, leading to mating type switching. Our approach can be adapted to other biological systems to study DSB repair with high precision, throughput and sensitivity.

## INTRODUCTION

Chromatin organization and positioning are nonrandom (1–5), and are fundamentally crucial for proper nuclear functions, such as gene transcription, DNA replication, and DNA breakage repair (6). These nuclear functions suggest that the spatial conformation of chromatin is highly dynamic and continuously reformed according to the physiological state of the cell, and cell populations are heterogeneous (2, 3, 7–9). DNA Double strand breaks (DSBs) are considered among the most genotoxic DNA lesions, leading to genomic instability if unrepaired. One of the main repair mechanisms is homologous recombination (HR), which exposes the lesion by resecting it to single strand DNA (ssDNA) overhangs to allow proximity with a homologous template for the synthesis of a new intact strand (10–13).

The mating type switching process in yeast involves a controlled DSB, and is thus used as a model system to study DNA damage repair mechanisms in eukaryotic cells. During the process, yeast cells switch between their mating types, namely 'a' (MATa) and 'α' (MATα), to allow sexual reproduction and diploidy (12). The difference between the two mating types is in the set of genes present in the MAT locus on chromosome III. The set is converted from one type to the other by means of HO-endonuclease DSB at the MAT locus, followed by repair by homologous recombination (HR), specifically gene conversion, using silent (unexpressed) templates on the same chromosome, namely HMLα and HMRa (14). As a model system for DSB repair, mating type switching sheds light on repair-related chromatin dynamics and biophysical properties in live cells (15–17), and novel imaging methods play an important role in further elucidating these processes.

Mating type switching studies typically use strains that lost their ability to switch, in order to allow controlled switching under induction in the lab. The switching process is most commonly controlled by the insertion of HO-endonuclease under a GAL promoter into the yeast genome and the induction of DSB by the addition of galactose to a medium containing raffinose or

lactate (18). Still, induced mating type switching is affected by various experimental conditions such as induction duration, cell cycle phase, chromatin perturbation due to genome editing, strain-dependent HO-endonuclease recognition levels, such as in the *MAT-stk* mutation, and population heterogeneity (12, 19–25); all of these factors can lead to reduced or unsynchronized switching. To overcome these hurdles, mutated strains or cell cycle synchronization are used to eliminate re-switching, for maintaining the switching levels (12). A different potential approach, that does not require such mutations, is using high throughput and sensitive assays to directly quantify and distinguish between switched and unswitched cells in the same culture at the single cell level in real-time.

Observations of DNA dynamics during mating type switching were previously done by labeling the HMLα and MAT loci with fluorescent repressor-operator systems (FROSs), and observing their locations over time (26, 27); operator repeat arrays were inserted into the genome near the loci, and were tagged by matching repressors conjugated to fluorescent proteins. Experiments using FROSs reported proximity events between the HMLα and the MAT loci that suggested contact, repair by gene conversion, and switching. However, this was done either in fixed cells (15, 28) or with very few live cells at low spatial resolution (for example, using a shared fluorescent protein for two systems, which limits the precision in which spatial co-localization can be determined) (15, 16). Thus, developing high throughput imaging methods with higher spatial and temporal resolutions for real-time DNA dynamics quantification in live cells would be valuable for better understanding the DNA damage repair process.

Here, we introduce high throughput methods for switching quantification and sub-nuclear imaging with high spatial and temporal resolutions in single live cells. We monitor switching occurrence in *S. cerevisiae* in real-time using both qPCR and a fluorescence reporter, and quantify the fraction of each mating type in the culture. Additionally, we demonstrate a simple label-free quantitative method, albeit with lower sensitivity, for real-time switching assessment, based on mating between opposite cell types, observed by flow cytometry (FC). Moreover, we quantify the negative effect of the introduction of FROS to the cells on switching frequencies, and show that it stems not only from genome editing, namely from integrating repeats next to HMLα and MATa, but also from the free fluorescent protein in the nucleus. Next, we demonstrate the applicability of point spread function (PSF) engineering microscopy for sub-

nuclear imaging, by observing population-level DNA dynamics at high temporal and spatial resolutions, in an imaging flow cytometer (IFC).

Imaging *MAT-stk* mutants with inefficient HO endonuclease activity that results in single and double strand breaks (SSB and DSB), in our high-throughput approach, enables detection of DNA damage associated loci movement as soon as 10 minutes after induction, which is earlier than previously reported (16, 28). Our results suggest two consecutive proximity stages between the HMLα and the MAT loci upon DSB induction: the first stage corresponds to DNA damage at the MATa locus leading to an immediate distance shortening, regardless of the type of damage (i.e. SSB or DSB), and the second stage resulting in a closer proximity between the loci that corresponds to DSB occurrence and repair by gene conversion.

## RESULTS

### High throughput real-time quantification of mating type switching in live cells

We developed quantitative methods for real-time live-cell monitoring and quantification of the mating type switching process based on either qPCR (constructing a calibration curve from known mixes of MATa and MATα cells; see methods and figure S3-C) or fluorescent reporter expression in switched cells using flow cytometry. To do so, we constructed switching and reporting plasmids, referred to as HO-CFP and HO-6XCFP, that include both a HO endonuclease gene under GAL10 promoter for DSB induction, and one or six fused repeats of CFP or msCFP fluorescent protein gene, respectively, under the MFα2 promoter for fluorescent reporting upon switching from MATa to MATα (figure 1A). Unlike a similar system that was constructed previously (16), here, the HO-endonuclease is expressed under the GAL10 promoter rather than GAL1 promoter (a stronger promoter (29, 30)), the coding genes are stably expressed (integrated into the genome), and the fluorescent reporter signal-noise ratio (SNR) is high due to localization of the fluorescent reporter into the nucleus by a nuclear localization sequence (NLS) and in the HO-6XCFP fusion of 6 msCFP units.

We transformed the BY4741 strain and induced mating type switching in liquid culture after initial growth in raffinose by the addition of galactose (2-4% w/v) to the media, prompting HO-endonuclease expression. To terminate HO-endonuclease expression, which has a short half-life time, of ~10 minutes (12), we added 2% glucose (w/v) after 1 hour of induction (figure

1B). We quantified switching after 6 hours from induction both by the CFP reporter (figure 1C), and by qPCR (figure 1D), and showed consistency between the two methods, that was kept among different colonies with different switching levels (figure 1D). Additionally, we compared the switching performance of our HO-CFP and HO-6XCFP plasmids to the pJH132 (31) and B2069 (16) centromeric plasmids in BY4741. Our plasmids resulted in 2-10 fold higher levels of switching (figure 1E). See section S1 and figure S5 in the supplementary material for more information about the validation of switching efficiencies.

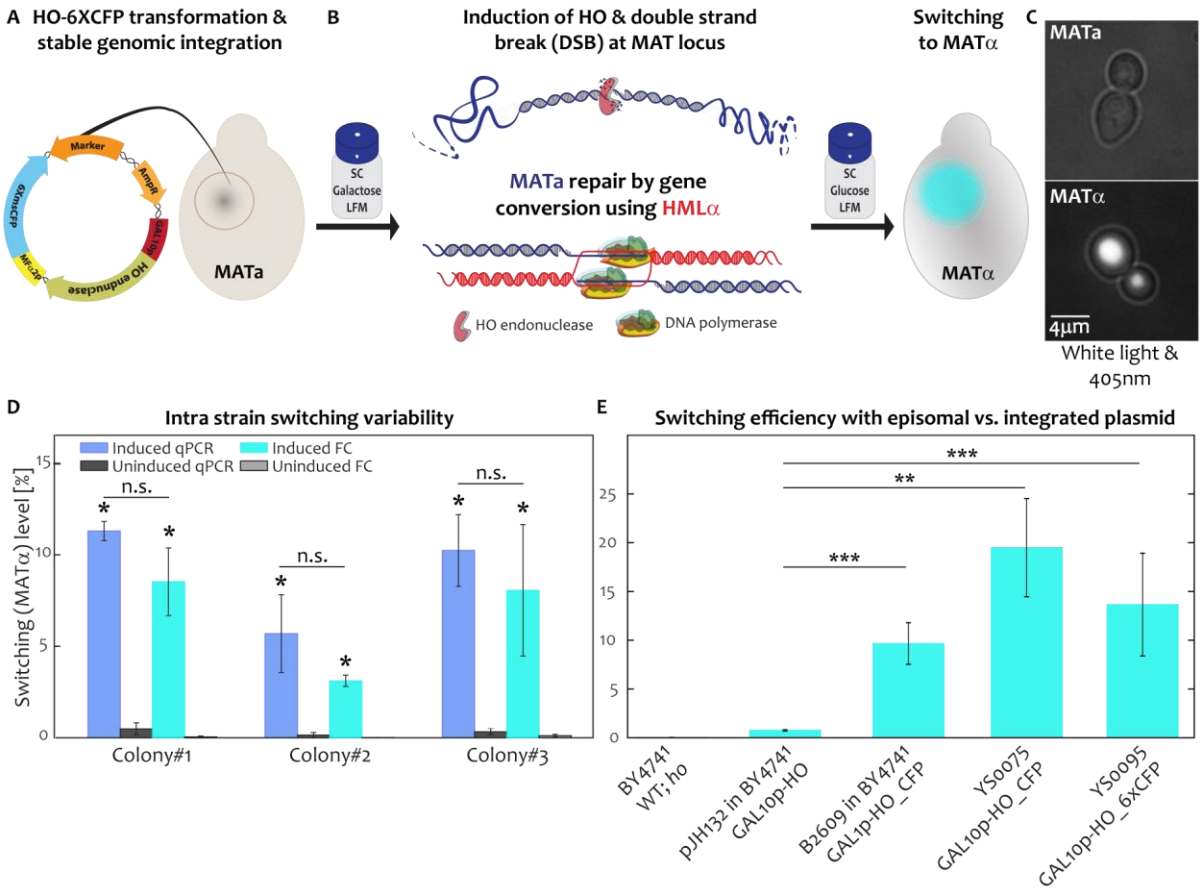


**Figure 1**. **Quantification of MATa switching to MATα**. (A) Construction of a mating type switching inducible strain, stably expressing the GAL10p-HO and MFα2p-6xmsCFP (YS0095; HO-6XCFP system). (B) Mating type switching involves DSB occurrence and repair by gene conversion, resulting in switching to the other type. Here, MATa cultures were induced by the addition of galactose for 1 hour. Induction was terminated by the addition of glucose, and (C) switching was reported by the expression of CFP, which was localized into the nucleus. (D) Switching levels 6 hours after induction, measured both by qPCR and flow cytometry (FC). Switching levels were significant comparing induced and uninduced cultures (*p-value* =0.0001), between colonies (*p-value*=0.0017), and non-significant (n.s.) between the two methods (*p-value* =0.2753). (E) Switching efficiencies of the HO-CFP and HO-6XCFP systems were compared to two centromeric plasmids. All experiments were done with at least 2 biological replicates.

We then monitored the switching process for 6 hours, collecting samples every 30-60 minutes: we followed DNA damage occurrence, including repair back to MATa type, i.e. repair that is not associated with switching, by qPCR with primers that span both the unique region and the HO cut site in the MATa locus (figure S3-A); we also quantified the switching level in the population using qPCR with unique primers for MATα type (figure S3-A) as well as the CFP-based method. The qPCR sensitivity enabled us to detect ~30% DNA damage after 30 minutes from HO-endonuclease induction, which increased to over 50% after 120 minutes, (figure 2A). The qPCR data suggested that switching occurred already as soon as 60 minutes after induction (figure 2B), earlier than implied previously for the W303 derived strains (70 and 105 minutes (21, 32), measured by qPCR and southern blot). We noticed that with different concentrations of galactose for induction (0, 2, and 4%) we achieved consistent results across the different methods, namely, qPCR (figure 2B) and CFP monitoring by IFC (figure 2C) and FC (figure 2D), overall achieving 6-10% switching at the end of the experiments.

The increase in MATa qPCR product towards the end of the experiments to ~60% (figure S3-D) indicated that at least 10% of the population did not switch to MATα type, and repaired the damaged DNA to MATa (figure 2A and figure S3-D), probably by HMRa as a template for gene conversion, by NHEJ (12, 33) or by canonical SSB repair pathways such as gap filling or ligation in case of partial cleavage at the *MAT-stk* locus (34). The rest 40% of the population, which were not MATa type, were composed of the 10% switched cells (MATα) and 30% that, we assume, either repair with the error prone mechanisms, namely single strand annealing (SSA) and alternative end joining (alt-EJ), or did not repair at all, the latter in agreement with previous studies (10, 35, 36). Overall, these results imply that the switching limiting step in the strain we used (BY4741 derivatives) is the DSB, in agreement with previous studies (12, 37).

In addition to switching quantification by CFP detection in flow cytometry, we were able to observe a negative correlation between the switching ratio and the number of singlets; as the population underwent switching, mating events occurred, manifested as doublet (non-singlet) events and observed in the forward and side scattering-channels as a reduction of singlet cells (figure S3-E). Indeed, calculating the fraction of switched cells expressing CFP in the singlet and in the non-singlet populations showed that non-singlet cells expressed CFP with significantly higher probability than singlets (figure 2E and figure S3-F). We approximate the switching level (Sw) by:

$$eq.1: Sw[\%] = \frac{\mathrm{X}}{\mathrm{Y} + 2\mathrm{X}} * 100\% - Bg$$

Where X is the number of non-singlets, Y is the number of singlets, and *Bg* is the non-singlet background percentage calculated using the uninduced culture. The calculation above assumes that each switched cell partners with an unswitched cell, manifesting as a non-singlet reading in the flow cytometer. We have found this approximation to be valid in the low switching level regime: the calculated switching levels over time (figure 2F) was similar to the qPCR, FC and IFC measurements. For example, at 300 minutes post induction we calculated 6.72% switching in the population, corresponding to 8.21%, 7.29% and 8.11% by qPCR, FC and IFC, respectively. Thus, simply counting singlet vs. non-singlets with a flow cytometer is useful as a label-free method to calculate mating type switching via mating. This detection method has a limited time frame: as the culture grows, aggregates form naturally, independent of mating events. This aggregation was visible in the uninduced culture plot, where there was a slight reduction in the number of singlets (figure S3-E), despite the lack of switching.

In summary, the methods for mating type switching detection that we optimized here are quantitative. The CFP-based method is live-cell monitoring compatible, fast and sensitive. The choice of method ultimately depends on the experimental requirements. For example, although the CFP-based methods report switching during the experiment, on the single-cell level, detection is lagging by approximately 90 minutes, due to the fluorescent protein expression time (38). The qPCR method, on the other hand detects switching after 60 minutes, however, it requires a tedious sample preparation procedure, including a genomic DNA extraction step. The different attributes of the methods are summarized in table 1.

**Table 1.** Features of mating type switching quantification methods developed in this study

| Feature | qPCR | CFP fluorescent marker | Label-free (FC) |
|---|---|---|---|
| **System preparation** | - Gal-HO plasmid design and cloning<br>- Transformation<br>- Design of mating type specific primers | - Gal-HO and CFP, mating type specific plasmid design and cloning: CFP expressed under MFα2-promoter for a-to-α and MFa1-promoter for α-to-a<br>- Transformation | - Gal-HO plasmid design and cloning<br>- Transformation |
| **Equipment** | qPCR system | Flow cytometry or fluorescence microscopy | Flow cytometry |
| **System calibration** | Yes | No | No |
| **Culture type** | Suspension | - Suspension<br>- Immobilized cells | Suspension |
| **Sample preparation/ processing time** | Genomic DNA extraction and qPCR reaction preparation (~2 days *) | Does not require special sample preparation, a few minutes simultaneously with experiment | No special sample preparation, a few minutes simultaneously with experiment |
| **On-line tracking of switching levels** | No | Yes | Yes |
| **a-to-α switching-detection lag-time** | <30 minutes | - 150 minutes (Suspension)<br>- 210 minutes (Immobilized cells) **<br>Depends on CFP expression and maturation time (39) | 120-150 minutes<br>Depends on the emerged MATα proteins expression |
| **Sensitivity** | 0.1% in the population | 1 cell | 1 cell |

* Sample preparation for quantification by qPCR depends on the size of the experiment; 3 biological replicates of 3 galactose concentrations (0%, 2%, 4%), sampled at 10 time points, ~2 day of preparation is required.

** Immobilized cells have additional switching lag of ~60 minutes due to the delay in medium replacement.

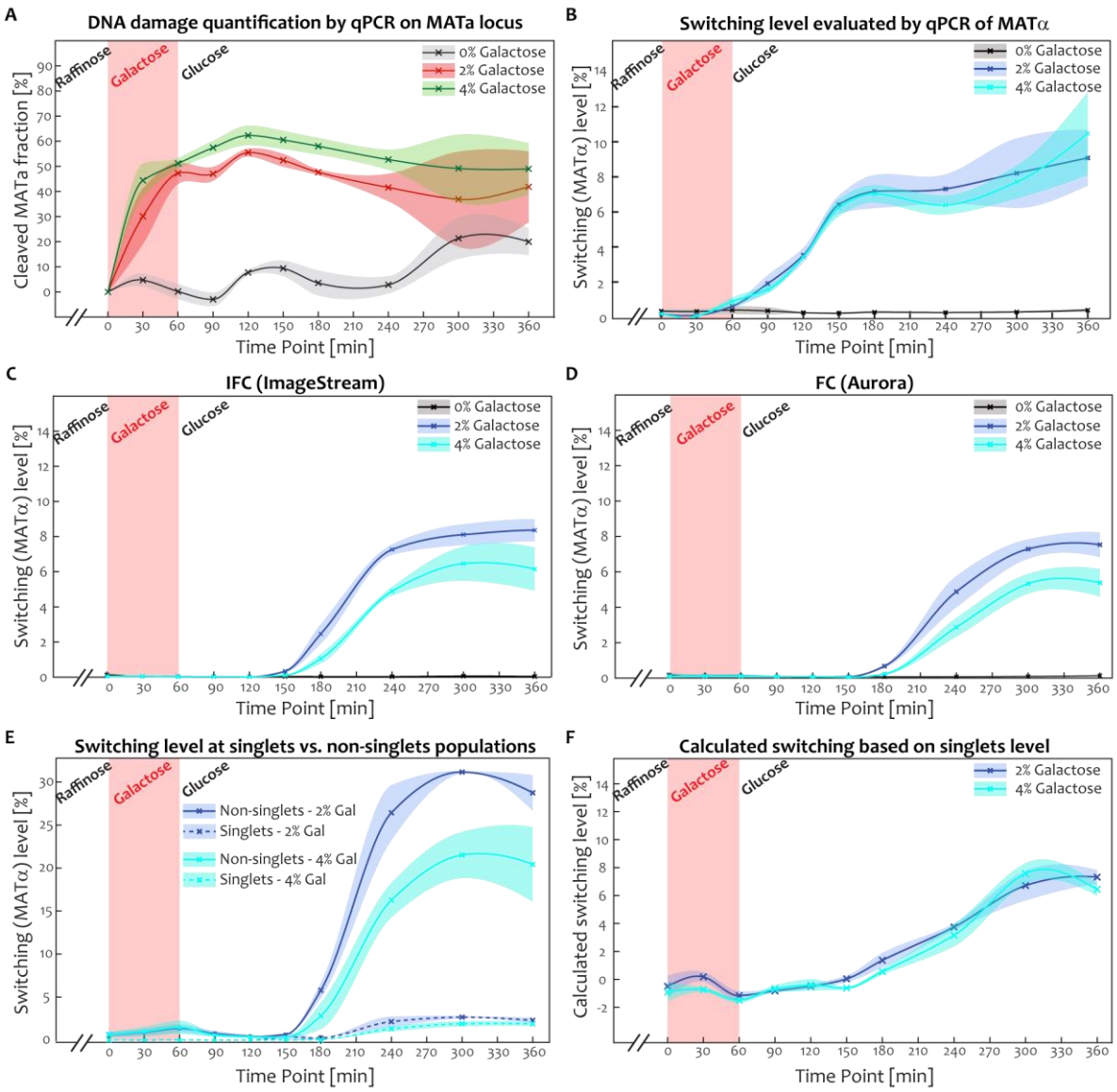


**Figure 2**. **Real-time tracking and quantification of MATa switching to MATα**. (A) qPCR of the MATa locus for DNA damage (disappearance of the MATa locus amplification) and non-switching repair (reappearance of MATa locus amplification) quantification (*p-value<<0.01)*. Tracking and quantifying switching using (B) qPCR of MATα locus, and CFP as fluorescent marker in (C) IFC, and (D) FC. Singlet levels found to be negatively correlated with switching levels, this was validated by (E) measuring and comparing the CFP levels (switched cells) in the singlets versus the non-singlets. based on this finding and using equation 5 we (F) quantified and plotted switching levels. All approaches obtained significant switching levels (*p-value<<0.01*) comparing induced to uninduced cultures, performed with either N-way or two-way ANOVA.

## Monitoring single cell switching in a high-throughput time-lapse microscopy

We employed a high throughput time-lapse microscopy combined with microfluidics to observe hundreds of cells from tens of FOVs over time and monitor switching events in single live cells. We used two microfluidic channels coated with ConA to immobilize cells onto the surface (16, 40), and conducted parallel assays for induced and uninduced cultures for 6 hours from induction (see Materials and Methods section for details). Cells were monitored for CFP expression in a HO-6XCFP strain (figure 3A). The induced population reached ~12% switching, similarly to the flow cytometry-based experiments, however, the CFP signal appeared later, after 210 minutes (figure 3B) compared to 150 minutes of a liquid culture (figure 2C-D). We assume that the delayed switching was the result of a slow medium exchange in the microfluidic channel (table 1). The main advantage of time-lapse microscopy over IFC is the ability to image the same cells over time. This enables real-time observation of mating events between switched cells (expressing CFP) and nearby neighbor of the other type (not expressing CFP). This supports the validity of CFP expression as a marker for switching (figure 3C and movie S1). As expected, CFP was visible in the diploid cells for at least 2 hours, in accordance with its half life time of ~2 hours (38), but not for longer, due to repression of transcription by the Mata1-Matα2 corepressor (12).

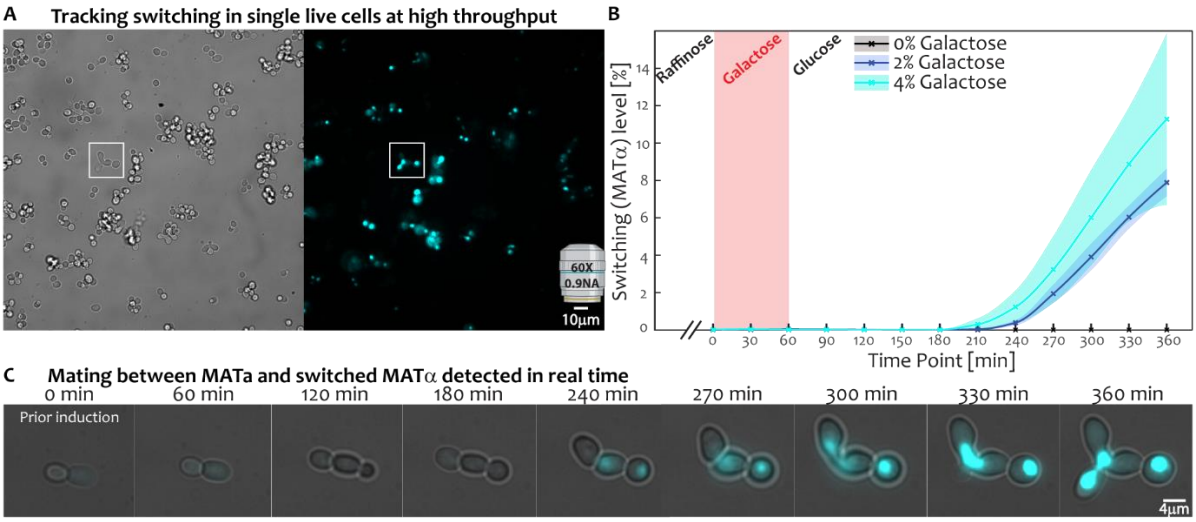

**Figure 3**. **Tracking switching in single live cells using time-lapse microscopy**. (A) Representative brightfield and 405nm images of yeast (YS0095), affixed to a microfluidic channel and induced for mating type switching, 360 minutes post induction. (B) Population switching level was quantified every 30 minutes for 6 hours by measuring CFP expression in cells in high throughput (hundreds of cells from tens of FOVs). (C) Tracking affixed single cells in the microfluidic channel over time with the fluorescent reporter in the MATα cell, illustrates *S. cerevisiae* homothallic life cycle: mating type switching, mating, and diploid cell budding.

**The effect of FROS on switching efficiency**

For live cell imaging of DNA dynamics during mating type switching, we used FROS (8) to generate observable fluorescent spots near the HMLα and the MAT loci (figure 4A) in a mating-type switchable strain, and measured the distances between the two localizations over time. The loci are expected to be in close proximity for the HMLα to serve as a gene conversion template after DSB induction, which initiates the switching process. FROS is a highly useful tagging approach for specific loci tracking in live cells, despite its limitations related to fluorescent background and spontaneous loss of operators (23). Specifically, when applying PSF engineering microscopy, it is critical to have high SNR since the photons are spread over a large PSF (41, 42). Thus we optimized new strains, rather than using existing ones (17, 28), for high fluorescent locus SNR. We found that eGFP (near the MAT locus; LacO, LacI-eGFP) and mCherry (near the HMLα; TetO, TetR-3xmCherry) outperformed YFP and mRFP with regard to SNR and spectral differentiation. Furthermore, to improve localization precision we screened for colonies with the highest SNR (see Materials and Methods and figure S1).

FROS integration into the yeast genome, while useful for localization microscopy thanks to the high SNR it provides, is expected to cause chromatin disruption, such as folding abnormalities (23); therefore, we quantified its effect on the efficiency of mating type switching. We compared switching efficiencies in HO-CFP strains that contained diffusing fluorescent proteins (i.e. no operator repeats), a single FROS, and two FROSs, and showed that insertion of the FROS indeed adversely affected the repair process during gene conversion and reduced switching efficiencies; however, interestingly, while the operators of the TetO-TetR (next to HMLα) caused reduced switching occurrence, in the LacO-LacI system (next to MAT) the reduced efficiency occurred mainly due to the free LacI-eGFP molecules, and the LacO-LacI

operators had a very minor effect (figure 4B). Overall, switching efficiencies were reduced by 2-3-fold, due to both the diffusing fluorescent proteins and the operator repeats.

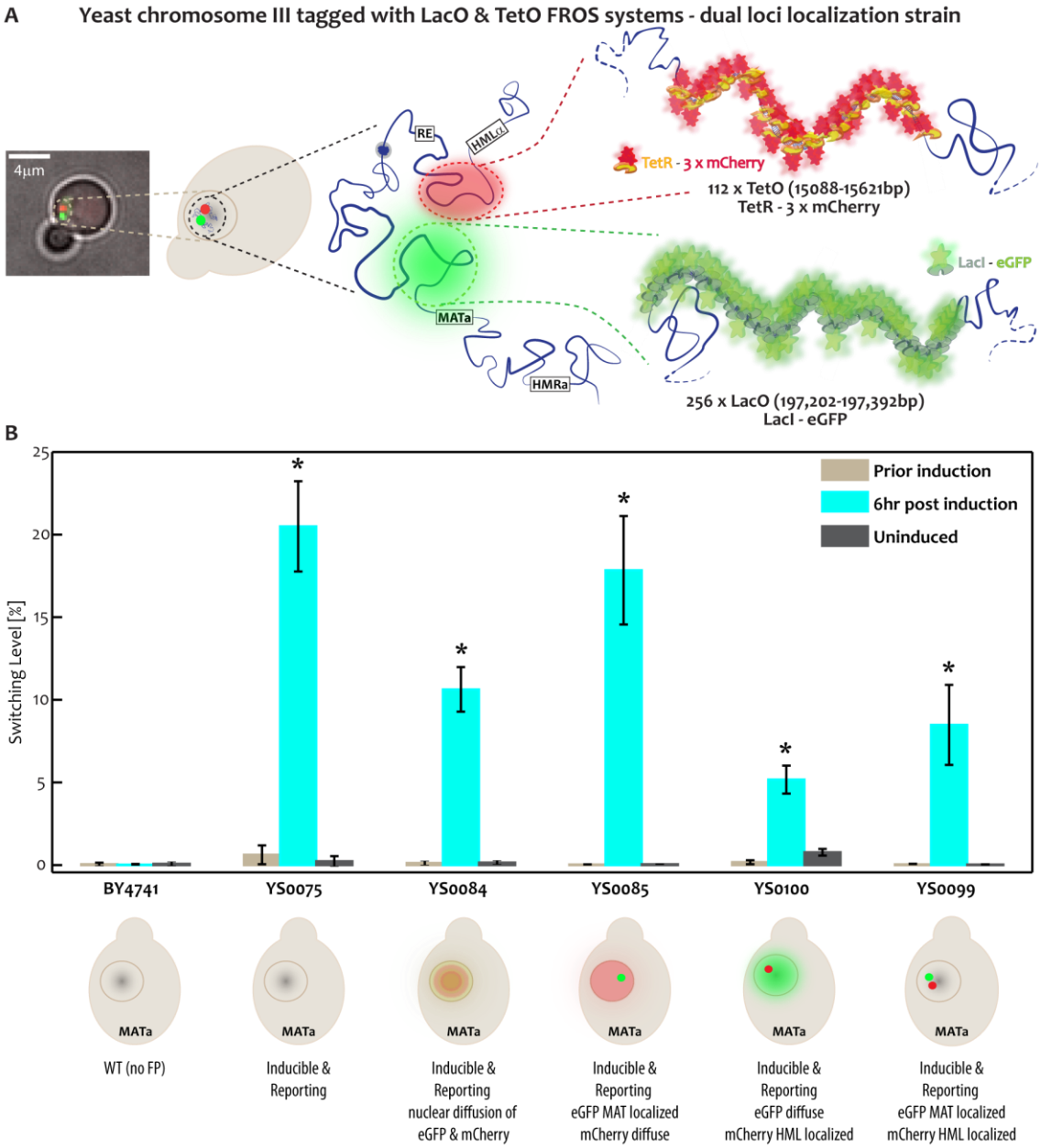


**Figure 4**. **Localization microscopy of mating type switching**. (A) FROS labeling of the mating type switching loci in live yeast cells. (B) The effect of FROS genome editing on mating type switching efficiency. The frequency of switching is significantly influenced both by genomic perturbations next to the MAT switching related loci, and the diffusing fluorescence repressor (*p-value*<<*0.01*; t-test).

**High-throughput analysis of DNA dynamics using IFC**

Combining flow cytometry with 3D nanoscale resolution and multi-color fluorescence imaging allows high-throughput data collection, and sub-nuclear visualization with high precision and accuracy at the single live cell level. We used the modified 3D IFC system (figure 5A-E) (43) to image thousands of cells per minute and to select cells with optimal locus threshold, i.e. good SNR spots, analyzing only 5-10% of the imaged cells, while maintaining statistical significance despite the low switching levels. Additionally, we demonstrated that employing 3D rather than 2D analysis is more precise when analyzing HMLα and MAT proximity, which is especially important for short distances, such as in the yeast nucleus (44), approximately 1.5 μm diameter depending on the carbon source (45), and since distances may change between cultures by as much as 150 nm due to natural heterogeneity (figure S6-A).

Initially we measured the native 3D distances between the HMLα and MAT loci, which were within the range of 300 to 470 nm across the same strain obtained in different transformations, implying heterogeneity in chromatin configuration (figure S6-A). We then proceeded to the switching experiments, acquiring images every 30 minutes (figure 5F, figure S6-B). We observed significant change in proximity between the fractured MATa locus and the HMLα template both in 2D and 3D analysis as soon as 30 minutes after induction (figure 5F), earlier than detected before (80 and 60 minutes (16, 28)).

According to our qPCR results, while 68% of the population experienced a DNA break event, (within 90 minutes), at the end of the experiment only 3.5% switched to MATα using HMLα as template (figure 5G, consistent with the CFP measurements in figure 5F). Additionally, 36% repaired to MATa type, by other means such as gene conversion with HMRa, NHEJ, and in case of nicked DNA by the canonical SSB repair pathways. And the rest of the population (~30%) that was detected neither as MATa nor MATα, repaired the damaged DNA by SSA, by alt-EJ or did not repair the damaged DNA at all (figure 5G). Although the dually FROS-tagged strain experienced ~15% more DNA damage compared to strain with no FROS (figure S3-D), we observed ~2.5-fold less switching to MATα (3-3.5% vs. 6-10%), and approximately 3.6-fold more cases of repair to MATa (36% vs. 10%), emphasizing the interference of FROS with the mating type switching process.

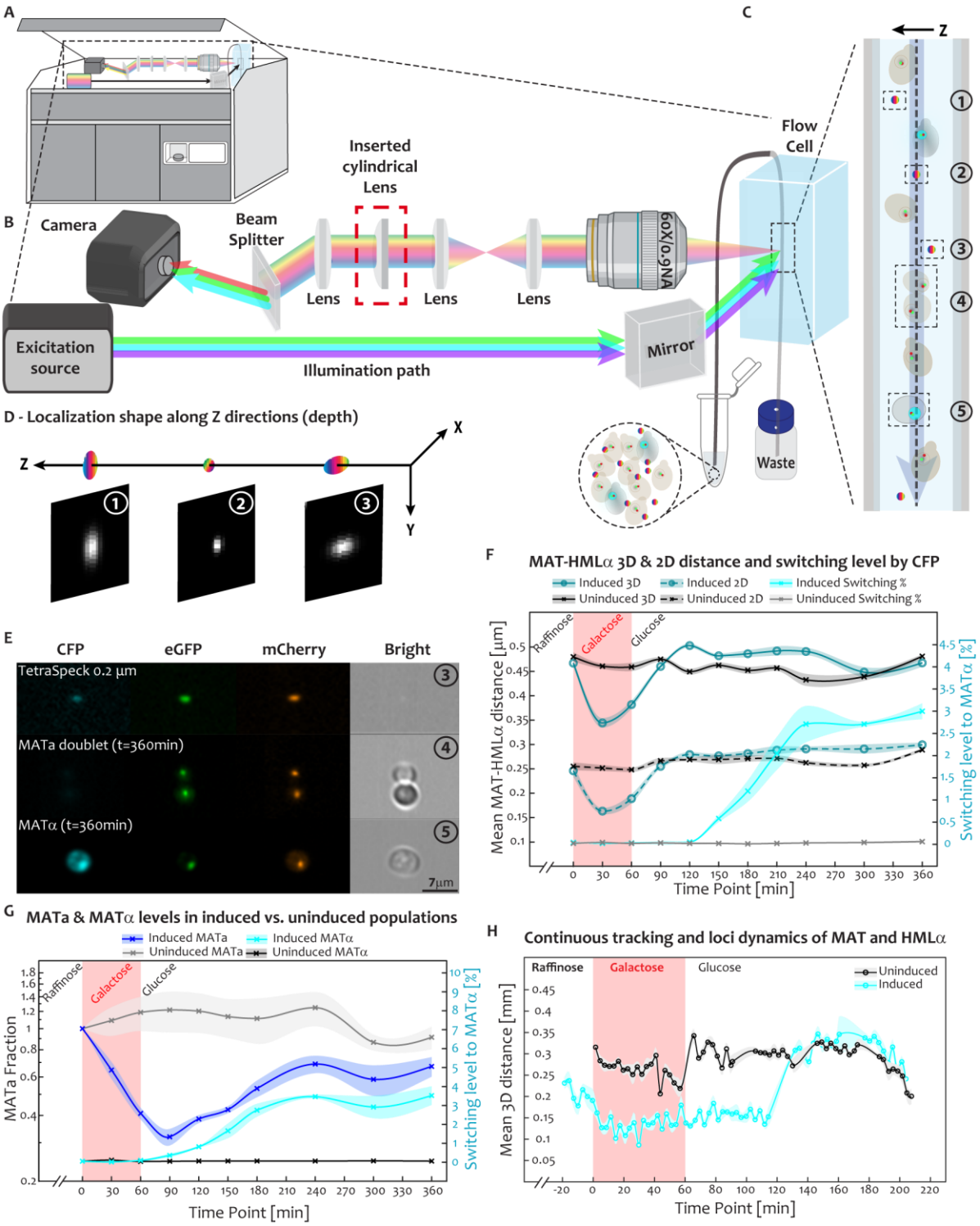
A
B
C
Camera
Beam Splitter
Inserted cylindrical Lens
Lens
Lens
Lens
60X/0.9NA
Flow Cell
Z
Exicitation source
Illumination path
Mirror
Waste
D - Localization shape along Z directions (depth)
X
Y
E
CFP
eGFP
mCherry
Bright
TetraSpeck 0.2 µm
MATa doublet (t=360min)
MATα (t=360min)
7µm
F
MAT-HMLα 3D & 2D distance and switching level by CFP
Induced 3D
Induced 2D
Induced Switching %
Uninduced 3D
Uninduced 2D
Uninduced Switching %
Raffinose
Galactose
Glucose
Mean MAT-HMLα distance [µm]
Switching level to MATα [%]
Time Point [min]
G
MATa & MATα levels in induced vs. uninduced populations
Induced MATa
Induced MATα
Uninduced MATa
Uninduced MATα
MATa Fraction
Switching level to MATα [%]
Time Point [min]
H
Continuous tracking and loci dynamics of MAT and HMLα
Uninduced
Induced
Mean 3D distance [mm]
Time Point [min]

**Figure 5**. **High throughput tracking of DNA dynamics** of the MAT and HMLα loci during switching. (A-E) IFC instrument setup and imaging: (A) ImageStream device illustration; (B) addition of a cylindrical lens for 3D acquisition; (C) beads were added to each of the culture samples for simultaneous 3D position calibration at each time point; (D) example images of bead PSFs at different 3D positions in flow (beads 1, 2, 3 in (C)) and; (E) image acquisition of a bead and cells in 4 channels: detection of switching occurrence by the CFP channel, 3D localizations of MAT and HMLα foci in the eGFP and mCherry channels, respectively, and object appearance by the bright field channel. (F) Real-time 2D and 3D distance measurements between MAT and HMLα, and switching levels by CFP detection of an induced and uninduced cultures (3 replicates were gathered and analyzed via bootstrapping: mean (line) ± s.d. (shaded region representing the estimated error) of eight independent groups in each time point, overall >542 cells per time point). Distance shortening and switching were detected 30 and 150 minutes, respectively, post DSB induction (*p-value* << 0.05). (G) DNA damage and switching levels for the dually tagged strain (YS0099) by qPCR (*p-value* < 0.01; 3 biological replicates). (H) Real-time distance between the MAT and HMLα loci during switching was assessed continuously for 3 hours, both in an induced and uninduced cultures. The 3D distances were divided and analyzed as 3-minute windows by bootstrapping: mean (line) ± s.d. (shaded region representing the estimated error) of eight independent groups in each time point with hundreds of cells in each frame. Statistical analyses were performed with two-way ANOVA.

Next, we repeated the switching experiment, but this time we observed distances continuously in time (figure 5H), rather than in 30 min batches. We observed similar behavior but at higher resolution: loci proximity was detected sooner, after 10 minutes from induction (in agreement with Hicks *et al*. (32), which reported DSB 10 minutes after induction in 50% of the population), and an average distance of ~150 nm between the loci (relative to 250 nm at t=0 and 300 nm in the uninduced) remained up to 2 hours (in agreement with Bressen *et al*. (15); figure 5G).

In all experiments, we did not find correlation between the initial distances (before induction) and the switching levels at the end of the experiment. In addition, despite the fact that the native distance between MAT and HMLα was larger in MATα than in MATa (figure S6-C and in accordance with (17, 46)), we did not observe overall larger distance in the switched population at the end of the experiment. This is to be expected, due to the low switching occurrence.

The discrepancy between the low switching levels (3-3.5%) and the striking distance shortening of ~120 nm (from 470 to 350 nm) between HMLα and MAT, observed 30 minutes after induction on the population level (figure 5F), calls for an explanation. Clearly, attributing this

distance shortening only to switched cells is not sufficient; this can be shown, first of all, by calculating the expected mean inter-loci distance in the population, even under the extreme assumption that 3.5% of the population is at distance 0 (i.e. the two loci are touching), at time points 30 and 60 minutes. The result is shown in figure 6A, on the uninduced population, exhibiting, as expected, a negligible effect on mean distances.

Secondly, we performed a cumulative distance cutoff analysis (figure 6B; see methods for more details and assumptions), from which we estimate that 70% of the population exhibit at some point, within the first 90 minutes, distances closer than 200 nm, which corresponds to the fraction of cells that underwent DNA damage according to our qPCR measurements. Furthermore, approximately 8.5-10% exhibited proximity of 80 nm or closer. This fraction coincides with the level of switching observed in a strain without FROS (figure 2B-D), suggesting that, possibly, this is approximately the population of cells that underwent DSB (assuming that in the FROS-free strain, switching rate following DSB is high).

This indirect analysis suggests the following dynamic model: immediately after DNA damage, induced by the HO-endonuclease (not necessarily a DSB), there is an initial proximity (200 nm cutoff) for 70% of the total population, followed by closer proximity (80 nm cutoff) for 8.6-10% of the total population, of which, 3-3.5% of the total population switched Thus, we conclude that the 80 nm cutoff may be indicative of DSB event.

To summarize, as illustrated in figure 6C, DNA damage event at the MAT locus, promotes an initial proximity between the HMLα and MAT loci, regardless of the type of damage or the presence of FROS. This is followed by a subsequent stage of enhanced proximity for cells that underwent DSB, resulting in physical association between HMLα and MAT and leading to switching. However, the effectiveness of switching is significantly diminished by the integration of FROS.

Overall, our high throughput 3D-informed computational analysis demonstrated greater sensitivity compared to other methods, achieving precise measurements of 3D distances at tens of nanometers scale (60- 80 nm, see figure S6-E and Materials and Methods). Combined with the other characterization methods presented here, this capability enabled us to differentiate between DNA dynamics associated with different type of DNA damage.

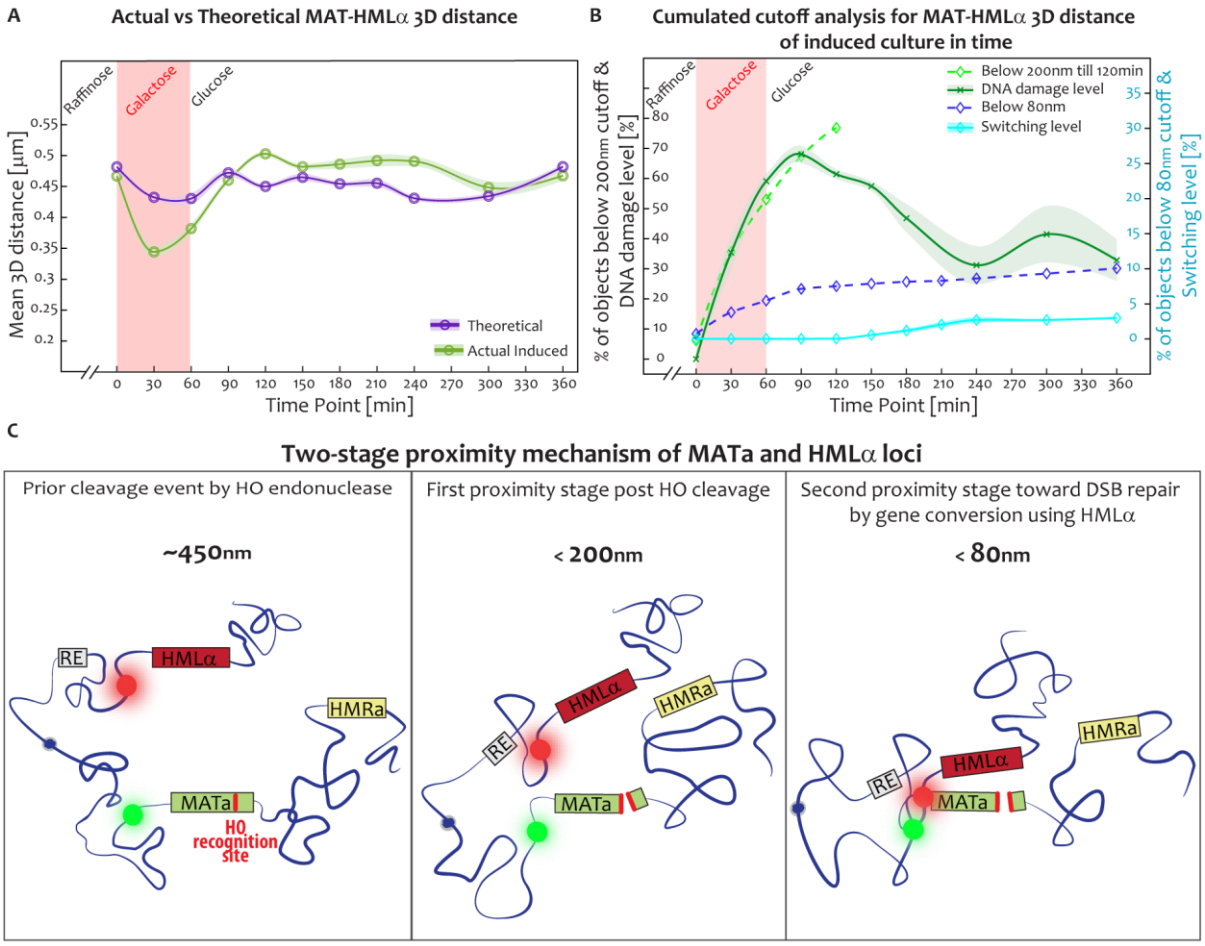


**Figure 6**. **MATa locus cleavage results in proximity between the HMLα and the MAT**. (A) IFC 3D distance analysis of induced culture compared to theoretical uninduced data with assumed 3.5% switching (distance 0). (B) Cumulative 3D distance cutoff analysis, including distances below 200 nm that correlate with DNA damage occurrence; and distances below 80 nm that correlate with DSB occurrence leading to mating type switching. (C) Suggested HMLα and MAT dynamics upon switching induction: intact chromosome 3 configuration with ~450 nm 3D distance between HMLα and MATa (left panel). MATa locus cleavage by HO results in HMLα and MATa movement to proximity <200nm (middle panel). Further movement and proximity to <80 nm (right panel) occur in cells with DSB (but not SSB) at the MATa, which promotes coupling of HMLα and MATa loci, repair by gene conversion and switching. Proximity distances are experiment and strain specific.

## DISCUSSION

### Advanced live cell analysis of mating type switching

In this work we presented high throughput methods for mating type switching investigation in live yeast cells. We used advanced biological, optical, and analytical tools to detect and follow switching occurrence and related DNA dynamics with high resolution and sensitivity, and revealed new findings.

Firstly, using quantitative real-time single live-cell analysis of switching occurrence with high throughput, we detected rare (single cell) switching events in a heterogenous population. We verified that the HO-endonuclease cut the MAT-*stk* locus inefficiently, as most of the DNA damage was not repaired by gene conversion. Additionally, we quantified and unveiled the negative influence of FROS tagging on the mating type switching process. Nevertheless, we showed that FROS, which serves as a popular DNA tagging for *in-vivo* tracking (47, 48), is still a valuable tool here, where its detrimental effect on switching rate can be compensated by using high throughput methods like those presented here.

Secondly, we demonstrated the potential of the high throughput 3D-IFC to study DSB repair dynamics. We monitored DNA dynamics with 2-3 fold higher spatial precision and accuracy than previously reported (60-80 nm compared to 200-300 nm (15–17, 46)). Importantly, the high throughput approach enabled imaging thousands of live cells, selected for optimal SNR, to observe mating type related loci during switching with high confidence, compared to fixed cells by confocal microscopy (28). Taken together, we observed two new findings upon mating type switching induction: 1. A movement that brings HMLα and MAT loci closer to each other as soon as 10 minutes after induction and; 2. Loose and tight proximities between the HMLα and MAT loci; the loose proximity occurred in cells that underwent DNA damage (either SSB or DSB) at the MAT locus, and the tighter proximity possibly correlates with DSB.

### Two-stage loci proximity mechanism for switching by gene conversion

We suggest a two-stage proximity mechanism for gene conversion between the HMLα and MATa loci. The first stage, which we term loose proximity and is observed as an inter-loci distance closer than 200 nm, includes a proximity promoting action by the cis-acting element, namely the recombination enhancer (RE), that brings the two loci closer to each other with the

aid of proteins that are bound to the RE (12). For example, the Fkh1 protein, which has multiple binding sites in the RE, and contains a conserved amino acid sequence, known as the FHA domain, interacts with phosphorylated DSB repair proteins during the mating type switching (12, 49–51). Based on our finding that switching rates are too low to explain the observed inter-loci proximities, , it is possible that Fkh1 binds phosphorylated SSB repair proteins near the damaged site as well (52–54). In addition, based on our results and on a previous study, which claims that resection initiates ~10 minutes after DSB formation (24), we suggest that the loci proximity, already seen 10 minutes after induction, happens independently to other phases of repair, namely resection, nucleofilament formation and search for homology by the DSB site (13).

The second stage, which we termed tight proximity, is observed as an inter-loci proximity closer than 80 nm where we suggest the probability of switching is increased, involves proteins which are relevant only for DSB repair (12, 13). This tight proximity may include multiple and reversible coupling events between the HMLα and MAT loci in each induced cell (16), that are probably interrupted in the dually tagged strain with the FROSs, which may explain the discrepancy between the 8.6% observed below 80 nm to the actual 3-3.5% switching level, but come in agreement with the switching level observed in strain without DNA tagging by FROS (figure 3B-F), in addition to the finite precision of our measurement. Further experiments with gene conversion related tagged proteins, such as Fkh1 or Rad51, and their effect on DNA dynamics the switching process will enhance the understanding regarding the sequential contribution of each protein in the complex DSB repair process in live cells.

Precise quantification, enabled here by high-throughput measurements, as well as monitoring of the switching process, are instrumental to the characterization of the different phenomena observed in this study; specifically, correct quantification of DSB among the total DNA damage, which could be wrongly attributed to mating type switching if switching levels were not monitored. As a future direction, differentiating between the dynamics of several repair mechanisms, such as HR and NHEJ can reveal differences between the processes and within it, that will enable to relate a specific event to a specific repair process.

## MATERIALS AND METHODS

### Plasmid construction

Plasmids used in this study are listed in table S1. The new plasmids were constructed by Gibson assembly (55), or by standard restriction and ligation using T4 ligase (M0202, NEB). Gibson fragments were amplified by polymerase chain reactions (PCRs) using either the PrimeSTAR GLX (R050A, Takara), LA Taq Hot Start (RR042A, Takara) or Q5 DNA (M0491, NEB) polymerase, with the appropriate primers (listed in table S2). All homologous recombination sites were amplified from *S. cerevisiae* (BY4741) genomic DNA, their locations are specified below. All plasmid modifications were validated by sequencing.

pYS0080 (CyPet expression under MFα2 promoter) was assembled by multiple Gibson steps using pUC19 backbone and DNA fragments amplified by primers P-YS1 to P-YS12 (pCyPet-His was a gift from Patrick Daugherty (Addgene plasmid # 14030 (56)); pYTK029 was a gift from John Dueber (Addgene plasmid # 65136 (57)); BS-Met15 was a gift from Zhiping Xie (Addgene plasmid # 69198 (58))); and the HR site was amplified from ChrXII (730361-730807 bp) with P-YS11 and P-YS12 primers. pYS0088 was assembled with pYS0080 backbone and CFP that was amplified from pIL01 (17) by PCR using P-YS13 and P-YS14 primers. pYS0099 was assembled with pYS0088 backbone and HO-endonuclease under the control of GAL10 promoter, namely, GAL10p-HO, which was amplified from pJH132 (31) by PCR using P-YS15 and P-YS16 primers. pYS0107 was constructed from pYS0099 backbone, which was amplified by PCR with P-YS17 and P-YS18 primers, and 6XmsCFP, which was extracted from YIplac211-SEC7-msCFPx6 (a gift from Benjamin Glick (Addgene plasmid # 105268) (59)), using EagI-HF (R3505, NEB) and NheI-HF (R3131, NEB) restriction enzymes.

pYS0019, carrying 112 TetO repeats with URA3 as a selection marker, was constructed from dually digested pKW2837 (8) with SacI (R3156, NEB) and NgoMIV (R0564, NEB) and HR site proximal to HMLα (15,088-15,621 bp, using P-YS19 and P-YS20 primers). pYS0020, carrying 256 LacO repeats with LEU2 as a selection marker, was constructed from dually digested pKW1689 (8) with Acc65I (R0599, NEB) and XhoI (R0146, NEB) and HR site proximal to HMRa (294,898-295,239 bp, using P-YS21 and P-YS22 primers). pYS0021 was constructed from dually digested pYS0020 with Acc65I and XhoI by replacing the HMRa HR site with HR site proximal to MAT (197,202-197,392 bp using P-YS23 and P-YS24 primers).

**Yeast strain construction**

All strains (listed in table S3) were derived from BY4741 & BY4742 (60), non-homothallic strains carrying mutated *ho*. BY4741 strain possesses the *MAT-stk* mutation, a single-base-pair substitution in the HO-endonuclease recognition site (T to A in Z11 (12, 37)). All strains were constructed by transforming linear plasmid (listed in table S1), digested by the appropriate enzymes, using the LiAc/SS carrier DNA/PEG method (61). The transformed strains were grown on the appropriate selectable medium, validated by colony PCR with primers listed in table S2, sequencing and by microscopy (figure S1-A). Moreover, we optimized our experiments by screening for colonies with the highest signal-to-noise ratio (SNR), using the IFC. We compared the SNR of each localization to a strain expressing the fluorescent proteins with no operator repeats, thus displaying lower SNR, and to 0.2μm TetraSpeck beads (TS200; T7280, Invitrogen), which display high SNR, leading to precise localization. The colonies with the higher fraction of cells above the SNR threshold, combined with two visual bright loci as observed by IFC, were chosen (figure S1-B).

The inducible and switching reporting strains YS0075 and YS0095, were constructed by transforming BY4741 with linear pYS0099 and pYS0107, respectively.

For dual-color tagging the MAT and HMLα loci, we used the LacI-LacO (26) and TetR-TetO (27) FROSs, respectively. First, YS0007, YS0020 and YS0084 were constructed by transforming BY4741, BY4742 and YS0075, respectively, with NheI-HF linearized pKW3034 plasmid (TetR fused to 3XmCherry and LacI fused to eGFP) (8). YS0104, YS0057 and YS0085 were constructed by transforming YS0011, YS0051 and YS0084, respectively, with PmlI linearized pYS0021 plasmid (256xLacO repeats). YS0011, YS0051, YS0099 and YS0100 were constructed by transforming YS0007, YS0020, YS0085 and YS0084, respectively, with BmgBI linearized pYS0019 plasmid (112xTetO repeats).

YS0096 strain was derived from YS0095 by switching induction and sorting twice CFP expressing cells (first sorting with Bigfoot Spectral Cell Sorter by Invitrogen, and second sorting with the FACSAria™ III Cell Sorter by BD). YS0096 MAT type was validated by colony PCR (with two sets of primers for the amplification of the MAT locus: P-YS41, P-YS42, P-YS43; see Table S2), microscopy, and mating.

**Media and growth condition**

All experiments started from a single isolated colony grown at 30°C and 200 rpm. For nonselective growth, we used standard YEPD medium (1% yeast extract (w/v), 2% bacto-peptone (w/v) and 2% dextrose (w/v)). For selective growth, we used defined SD medium (0.67% YNB without amino-acids (AA) (w/v) and 2% dextrose (w/v) supplemented with all necessary AA and nucleobases according to strain requirements; as indicated in Cold Spring Harb Protocol (62). We added 1.5% bacto-agar (w/v) for petri dish growth). For microscopy visualization cells were grown in liquid defined SC low fluorescent medium (LFM) (0.69% YNB (without AA, folic acid, and riboflavin) (w/v), all necessary AA and nucleobases according to requirements, and supplemented with 2% carbon source (raffinose/ galactose/ dextrose) (w/v)).

Importantly, we used the same medium for the starter and culture to avoid hindrance of the fluorescent proteins expression, since we found the FROS system to be sensitive to media change; when we used YEPD starters for raffinose culture, localizations were poor and, in some cases, invisible.

**Mating type switching by galactose induction**

Single isolated colonies were grown in 2ml SC-2% Raffinose (LFM) media for 2-7 days at 30°C and 200 rpm for sufficient cell density. Cultures were resuspended in fresh SC-2% Raffinose (LFM) in baffled erlenmeyer for additional O/N incubation, to reach optical density at 600 nm ($O.D_{600}$) ~0.25-0.35 (about $10^7$ cells/ml), which was just before entering logarithmic phase at time of induction (t=0); $O.D_{600}$ was measured using Ultrospec10 spectrophotometer (Biochrom). The culture was then divided into two baffled erlenmeyers, for switching induction by galactose culture (induced culture), and for control without induction culture (uninduced culture), which were incubated at 30°C and 200-250 rpm throughout the experiment. Switching was induced by adding stock solution of 20% galactose to the culture (2% (w/v) final concentration in culture), which was terminated after 60 minutes (unless specified differently) by adding 40% glucose stock solution (2% (w/v) final concentration in culture). Samples were collected for analysis by IFC, Flow Cytometry (FC), and qPCR before, during, and after induction, at 30-60 minutes intervals and up to 6 hours post induction. For mating type switching induction in a microfluidics channel see below for more details.

**Mating type switching analysis by flow cytometry (FC)**

Yeast culture samples (200-600µl) during the switching experiments were analyzed using the Cytek Aurora full spectral FC device. Data analysis was done using the SpectroFlo software. 'Cells for analysis' were gated using SSC-H X FSC-H, and 'singlets' were gated using SSC-H X SSC-A (Figure S2-A-B). CFP expressing cells (switched from MATa to MATα) were gated based on the unstained culture (BY4741), the culture before induction (YS0095) and a CFP positive strain (YS0096) (Figure S2-C-E).

**Mating type switching analysis by qPCR**

5 ml culture samples were obtained during the switching experiments for genomic DNA (G-DNA) extraction by precipitation as follows: Cells were centrifuged for 5 minutes at 1,377 rcf, harvested and resuspended in the minimal medium left after removal of most of the supernatant; G-DNA was precipitated using MasterPure Yeast DNA Purification Kit (MPY80200) according to the kit protocol with the following modifications: centrifugation steps were done in 4°C, microtubes were left open for 15-20 minutes to ensure 70% ethanol evaporation, and DNA pellets were resuspended in 50-100 µl MBW.

For switching and DNA damage quantification, each G-DNA sample was analyzed by qPCR with three sets of primers (Figure S3-A): 1. P-YS41 and P-YS42 (17) for MATα genomic region, 2. P-YS42 and P-YS43 (17) for MATa genomic region, and 3. P-YS44 and P-YS45 for ACT1 region (housekeeping gene). Based on primer calibration assay (figure S3-B), G-DNA samples were diluted to 5 ng/µl. Each qPCR reaction contained 6.8 µl MBW, 10 µl PerfeCTa SYBR Green FastMix Low ROX (2X), 0.6 µl (10 µM) of each primer (forward and reverse), and 2 µl G-DNA (10 ng). We used a standard qPCR cycling protocol (QuantStudio1, Applied Biosystems) with initial denaturation stage (3 minutes, $95^0$C), 40 amplification cycles (15 seconds, $95^0$C), end of extension stage (1 minute, $60^0$C) and a dissociation stage. Raw Ct data was analyzed to assess fold enhancement (switching) and reduction (DNA damage) using pfaffl method (63). To quantify switching levels we plotted standard curve based on multiple known mixes of BY4741 (MATa) and BY4742 (MATα) cultures: stationary phase cultures at the same $O.D_{600}$ were mixed, and immediately their G-DNA extracted to avoid mating events; the samples were analyzed by qPCR with MATα primers, and; the Ct values were used to a generate standard curve in the range of 0.5%-30% MATα (figure S3-C). MATa switching events to MATα were accurately

quantified by fitting the Ct values to the standard curve equation. DNA damage levels were assessed with MATa primers (P-YS42 and P-YS43), based on the knowledge that different DNA lesions intrude the polymerase and reduce amplification (64), which was calculated relatively to the housekeeping gene (ACT1) and the starting point (prior induction).

**Imaging Flow cytometry (IFC)**

*Instrument setup.* High throughput live cell 3D imaging was done using the ImageStream®X Mark II (Amnis) IFC, modified by the insertion of a cylindrical lens ($f$=1m, LJ1516RM-A, Thorlabs), which was mounted by kinematic magnetic bases (KB2X2, Thorlabs) into the optical path as described previously (43). We used the following device settings: (1) 60X/0.9NA objective, (2) turning off autofocus and determining manually the ideal focal position for each run, (3) operating 3 lasers: 405 nm (120 mW) for CFP detection in channel 1, 488 nm (200 mW) for eGFP detection in channel 2, 561 nm (200 mW) for mCherry detection in channel 4, and (4) operating the brightfield illumination in channel 6.

*Data acquisition*. Induced followed by uninduced live cell culture aliquots (200 µl) were mixed with 0.2 µm TetraSpeck beads (0.2 µl; diluted by 1000), flowed and imaged prior to induction (defined as t=0), every 30 minutes for 4 hours, and after 5 and 6 hours post induction (11 time points in total).

As a first pre-processing step, the brightfield channel helped us to distinguish between bead images and cell images. We then gated images that contained intact singlet and doublet cells (area <80, aspect ratio >0.35), in focus (gradient RMS>50), and high SNR (discarding noisy cells by 'raw max pixel' for channel 2 and channel 4). These cells were analyzed for CFP expression by 'intensity' and 'raw max pixel' in channel 1 for real-time switching occurrence (Figure S4-A). Next, we exported the bead images and the high SNR cell images into rif, cif, daf and txt files, beads data for calibration, and cells data, generated by the ISX and the IDEAS software, for 3D distance analysis. The rest of the analysis was done by an automatic analysis pipeline written in publicly available online (65), and divided into four main parts: 1) pre-processing of the cif data; 2) calibration of PSF shapes to z positions by beads; 3) 3D localization estimation by Gaussian fitting; 4) 3D distance prediction.

*Pre-processing and parameter initialization.* The first step in our analysis pipeline involved converting the cif file to a tif format. Additionally, we performed mean intensity padding to the maximal image size in the cif data and normalized the pixel intensities per image to be in the range [0, 255]. We repeated this step twice: for the green channel (channel 2), and for the red channel (channel 4).

Next, we initialized some parameters according to our ImageStream device, such as: the pixel size, the diameter of the flow tube, etc. We also determined the minimal signal-to-noise ratio (SNR) that was required from an image to enter the analysis pipeline. We used this threshold since locus localization for images with low SNR was less accurate and hindered the ability of our pipeline to detect small inter-loci distance changes over the cell population.

*Calibration by beads.* To obtain the 3D positions of the loci inside the cells we used a cylindrical lens for PSF engineering. When imaging with a cylindrical lens, the PSFs are gradually stretched as a function of their z position in along different axis above and below the focal plane. To relate each PSF shape (width and stretch direction) to a specific z position, we performed calibration between the PSF shape and the z position of the locus.

We found out that performing calibration by the images of labeled loci inside cells presented challenges due to background noise and low SNR. Therefore, we performed the calibration using fluorescent beads, characterized by their high SNR and lack of cell background noise (Figure S4-B).

Each bead PSF was fitted to a 2D asymmetric gaussian model denoted by eq.2:

$$eq.2:\ \ AsymGauss(x,y) = offset + \frac{A}{2\pi\sigma_x\sigma_y} \cdot e^{-\frac{(x-x_0)^2}{2\sigma_x^2} - \frac{(y-y_0)^2}{2\sigma_y^2}}$$

Where: *offset* is the mean background value, $A$ is the amplitude, $\sigma_X$, $\sigma_Y$ are the gaussian standard deviation estimates, and $x_0$, $y_0$ are the bead location estimates.

We drew a histogram of the predicted $\sigma_X$, $\sigma_Y$; then, we calibrated the histogram of each sigma to the z position of the bead, namely, we ended up with two calibration functions, one for each axis. Similar to previous work (43), we assumed the bead position in each axis inside the flow cytometer was approximately normally distributed with 95% of the beads within a cylinder with radius of 2.2 μm. Hence, we could fit each sigma histogram to normally distributed

positions in the z axis (Figure S4-C). First, we counted the total number of recorded beads, N. This allowed us to know the expected number of sigma values observed for each interval in the z axis. We drew the expected sigma counts in 50 nm resolution along the z axis inside the range [-2.2μm, 2.2μm] according to the normal distribution assumption. We fitted $\sigma_X$, $\sigma_Y$ histograms to the expected counts in z axis and obtained two calibration functions. During the localization stage of our pipeline, we used the mean estimation of z position of these two calibration functions.

Optimally, the PSF is the smallest when the cell is in focus and there is an equal number of beads above and below focus; however, the focus might change unintentionally over long acquisition periods leading to asymmetric empiric distribution. Therefore, during the calibration we divided the beads to two groups: horizontally stretched beads and vertically stretched beads. Then, we calculated the expected farthest bin we observed in the Gaussian distribution, namely, we shifted the center of the Gaussian distribution to the real focal plane.

*3D localization prediction in cells.* We performed 3D localization analysis in the red and the green channels separately for each cell image. The localization process was composed of the following steps: 1) images were cropped to a constant size ($25\text{x}25 pixels^2$ or $7.5\text{x}7.5[\mu\text{m}^2]$); 2) images with bad SNR (SNR<15) were filtered out, where SNR was defined by the max intensity pixel value divided by the mean pixel value in each image; 3) each local maxima was fitted to a the model , described in eq. 3, of an asymmetric Gaussian (depicting the PSF engineered locus) overlapping a rotated asymmetric Gaussian (depicting the cell background); 4) $x, y$ position of the cells were extracted from the locus Gaussian fit parameters; 5) the predicted $\sigma_X$, $\sigma_Y$ parameters of the locus Gaussians were used to predict the z position.

$$eq.3:\ \ GaussOnGauss(x,y) = OS(x,y) + \frac{A_1}{2\pi\sigma_x\sigma_y} \cdot e^{-\frac{(x-x_0)^2}{2\sigma_x^2} - \frac{(y-y_0)^2}{2\sigma_y^2}}$$

Where: $OS(x,y)$ is the offset defined by the cell background (see eq. 4), $A_1$ is the locus amplitude estimate $\sigma_X$, $\sigma_Y$ are the locus Gaussian standard deviation estimates, and $x_0$, $y_0$ are the locus location estimates.

$$eq.4:\ \ OS(x,y) = offset + A \cdot e^{-\left(a\cdot(x-X_0)^2 + b\cdot(x-X_0)(y-Y_0) + c\cdot(y-Y_0)^2\right)}$$

Where: *offset* is the mean background signal in the image, A is the cell amplitude estimate, $\sigma_X$, $\sigma_Y$ are the cell Gaussian standard deviation estimates, $x_0$, $y_0$ are the cell location estimates, and a, b, c are the parameters of an asymmetric gaussian rotated by the angle $\theta$:

$$a = \frac{\cos^2(\theta)}{2\sigma_X^2} + \frac{\sin^2(\theta)}{2\sigma_Y^2}, b = -\frac{sin(2\theta)}{4\sigma_X^2} + \frac{\sin(2\theta)}{4\sigma_Y^2}, c = \frac{\sin^2(\theta)}{2\sigma_X^2} + \frac{\cos^2(\theta)}{2\sigma_Y^2}$$

If the $R^2$ fit score was less than 0.9, we removed the locus from the analysis pipeline. Finally, we used the precalculated calibration functions for $\sigma_x$ and $\sigma_y$ and averaged their predictions to get the final estimate of the z position.

*3D distance prediction.* In this study, we reported the mean 3D distance values of the analyzed cell population at each time point. The 3D distances between the loci in the green channel and the red channel per cell was calculated by $L_2$ distance (eq. 5):

$$eq.5:\ \ Distance_{3D} = \sqrt{\left(x_{green} - x_{red}\right)^2 + \left(y_{green} - y_{red}\right)^2 + \left(z_{green} - z_{red}\right)^2}$$

In cases where there were multiple loci in a single image, we validated that the number of loci detected was the same in both channels, otherwise the cells were filtered out from the analysis. Furthermore, we did not analyze loci that were located within distances of 5 pixels to avoid ambiguity due to extremely large PSFs.

The ImageStream device detects different cells in different positions due to flow rate variability over time and space. Namely, different cells are detected in different positions on the ImageStream sensor. To overcome biases in the predicted position due to the cell position relative to the sensor, we applied mean subtraction of the mean predicted x, y positions from each cell's predicted x, y positions. Notably, this step substantially improved the performance of our pipeline, i.e. the bead distance histograms got closer to zero after applying this step.

*Cumulative distance cutoff analysis.* To quantitatively correlate between the level of DNA damage and MATa - HMLα distances we performed a cumulative cutoff analysis, where we sub-grouped the population according to defined maximal distances, namely cutoffs, under two assumptions: (1) we assumed that MATa – HMLα proximity in each analyzed cell was observed only once during the assay; and (2) this shortening lasted up to 30 minutes (the interval between each time point; and in agreement with Houston & Broach (16)). The first

cutoff was calculated according to distances that matched in number to the levels of DNA damage which was quantified by qPCR up to 90 minutes after induction (the relevant time window where HO is expressed and rapidly degraded (12)). The second cutoff was calculated according to the switching levels in FROS-free strains (exhibiting a maximum switching efficiency) as an indicative measurement of attempts of DSB repair by gene conversion. We validated that this cutoff is within the precision range of our method (figure S6-D).

**High throughput time-lapse microscopy**

*Microfluidic slide preparation*. We coated two channels in a glass-bottom microfluidic VI 0.5 µ-Slide (Ibidi, 80607) with Concanavalin A (ConA; C2010, Sigma-Aldrich); the lyophilized ConA powder was dissolved in 80% double distilled water (DDW), 10% PBS pH=6.5, 5% 1M $CaCl_2$ (C5080, Sigma-Aldrich) and 5% 1M $MnCl_2$ (M3634; Sigma-Aldrich) to 20 mg/ml (40) and kept at -80$^0$C; Before usage, 200 µl ConA aliquot was gently thawed on ice and mixed with 700 µl DDW and 100 µl PBS (x2) pH=6.5, reaching final concentration of 4 mg/ml; 140 µl of the ConA mixture was loaded into the two microfluidic channels, incubated for 12-15 minutes at room temperature, and washed twice with 140 µl DDW. For the inoculation, 140 µl of yeast culture at $O.D_{600}$~0.25-0.35 (see Mating type MAT switching by galactose induction section) were loaded into the two channels. The two microfluidic channels were then connected by silicone tubes (Tygon silicone tubing, 1/32"ID x 3/32"OD, Cole-Parmer) to media reservoirs: the uninduced channel was connected to SC-2% Raffinose (LFM) reservoir; the induced channel was connected via a bidirectional valve (M-Switch MSW002, Fluigent, controlled by OxyGEN software) to allow sequential flow into the channel of SC-2% Raffinose (LFM), SC-2% Galactose (LFM) and SC-2% Glucose (LFM). The media were connected to Flow EZ system equipped by LU-FEZ-00345 and LU-FEZ-01000 controllers (Fluigent), for controlled medium injection into the uninduced and induced channels, respectively.

*Mating type switching induction*. Yeast culture was loaded into two microfluidic channels, one for induced culture and the other for uninduced (control). Following the initial imaging sequence with cells in SC-2% Raffinose (LFM), the medium in the induced channel was shifted to SC-2% Galactose (LFM) using the M-switch valve. After one hour, the medium was shifted again to SC-2% Glucose (LFM) to terminate HO-endonuclease induction.

*Optical setup*. We used a fluorescence microscope (Nikon, ECLIPSE Ti) equipped with NIS software, an iChrome MLE system combining 405, 488, and 561 nm lasers (Toptica), a NIDAQ card (NI PCI-6723 32 ch Analog Output Board) and a PRIOR Piezo stage. The emission path includes a multiband pass dichroic mirror (405/488/561/647 nm, TRF 89902-NK, Chroma), and a sCMOS camera (Prime 95B, Photometrics) with a 50-60 millisecond exposure time. NIS-Elements AR Auto Research Software (5.02.02) was used to trigger sample illumination upon data acquisition. For CFP tracking we used a 60x air objective (Plan Apo lambda 60x/0.95 WD 0.11-0.21, Nikon).

*Single cell tracking and quantification of mating type switching*. Live cells from 40-50 field of views (FOVs) were tracked, both in the induced and the uninduced microfluidic channels at 30 minutes intervals over six hours of switching experiments. Using the Photometrics camera and the NIS software we trigger the sample illumination with a series of 405 nm to detect the CFP expression in switched cells, and white light illumination for brightfield images.

CFP reporter image analysis was performed using ImageJ and Matlab. For each FOV and time point, we conducted cell segmentation using the autofluorescence of the cells with a "StarDist" network (66) trained on 10 images from the experimental dataset to enhance its accuracy, creating a new "StarDist" model. The segmentation was performed using the "StarDist 2D" plugin in Imagej, with appropriate probability threshold and overlap threshold matching the mask to cells in the images. From the segmented images, masks were generated in Matlab and applied to the original 405 images after background subtraction, and the average fluorescence intensity was measured for each cell individually. For each time point and FOV, the average intensity of all cells was calculated, and the fluorescence intensity was averaged across all time points for each condition (induced and uninduced). The percentage of cells that underwent switching was calculated based on a predetermined threshold intensity value determined according to the fluorescence intensity of the cells at time t=0 (prior to induction) in both microfluidic channels, and at t=6 hours in the control (uninduced) channel.

## DATA AVAILABILITY

The data underlying this article will be shared on reasonable request to the corresponding author.

## SUPPLEMENTARY DATA

Supplementary Data are available online.

## AUTHOR CONTRIBUTIONS

Yael Shalev Ezra: Conceptualization, Methodology, Visualization, Data analysis, Writing—original draft. Alon Saguy: Data analysis. Gaia Levin: Methodology, Data analysis, Visualization, Lucien Weiss: Methodology. Onit Alalouf: Conceptualization, Supervision, Methodology, Writing. Yoav Shechtman: Conceptualization, Supervision, Methodology, Writing.

## ACKNOWLEDGEMENTS

We would like to thank Dr Elisa Dultz, Prof. Karsten Weis, Prof. Kerstin Bystricky, Prof. James R. Broach, Prof. James E. Haber, Prof. Nabieh Ayoub and Prof. Yoav Arava for providing us with plasmids, yeast strains and very valued advice and discussions.

We also would like to thank Maayan Duvshani, Yosuf Mansur, and Aviv Lutaty and the Life Science and Engineering (LS&E) Infrastructure Center for the technical assistance with the flow cytometry devices.

## FUNDING

This work was supported by the European Research Council (ERC) under the European Union Horizon 2020 research and innovation program [grant number 802567 to Y.S.].

## CONFLICT OF INTEREST

The authors declare no conflict of interest.

## REFERENCES


1. Taddei,A., Schober,H. and Gasser,S.M. (2010) The Budding Yeast Nucleus. *Cold Spring Harb Perspect Biol*, **2**, a000612.

2. Misteli,T. (2005) Concepts in nuclear architecture. *BioEssays*, **27**, 477–487.

3. Dultz,E., Tjong,H., Weider,E., Herzog,M., Young,B., Brune,C., Müllner,D., Loewen,C., Alber,F. and Weis,K. (2016) Global reorganization of budding yeast chromosome conformation in different physiological conditions. *J Cell Biol*, **212**, 321–334.

4. Batut,P.J., Bing,X.Y., Sisco,Z., Raimundo,J., Levo,M. and Levine,M.S. (2022) Genome organization controls transcriptional dynamics during development. *Science*, **375**, 566–570.

5. Bickmore,W.A. and van Steensel,B. (2013) Genome Architecture: Domain Organization of Interphase Chromosomes. *Cell*, **152**, 1270–1284.

6. Gibcus,J.H. and Dekker,J. (2013) The hierarchy of the 3D genome. *Mol Cell*, **49**, 773–782.

7. Finn,E.H. and Misteli,T. (2019) Molecular basis and biological function of variability in spatial genome organization. *Science*, **365**, eaaw9498.

8. Dultz,E., Mancini,R., Polles,G., Vallotton,P., Alber,F. and Weis,K. (2018) Quantitative imaging of chromatin decompaction in living cells. *Molecular Biology of the Cell*, **29**, 1763.

9. Gasch,A.P., Yu,F.B., Hose,J., Escalante,L.E., Place,M., Bacher,R., Kanbar,J., Ciobanu,D., Sandor,L., Grigoriev,I.V., *et al.* (2017) Single-cell RNA sequencing reveals intrinsic and extrinsic regulatory heterogeneity in yeast responding to stress. *PLOS Biology*, **15**, e2004050.

10. Ceccaldi,R., Rondinelli,B. and D'Andrea,A.D. (2016) Repair Pathway Choices and Consequences at the Double-Strand Break. *Trends Cell Biol*, **26**, 52–64.

11. Sugawara,N. and Haber,J.E. (1992) Characterization of double-strand break-induced recombination: homology requirements and single-stranded DNA formation. *Mol Cell Biol*, **12**, 563–575.

12. Haber,J.E. (2012) Mating-Type Genes and MAT Switching in Saccharomyces cerevisiae. *Genetics*, **191**, 33–64.

13. Aylon,Y. and Kupiec,M. (2004) New insights into the mechanism of homologous recombination in yeast. *Mutation Research/Reviews in Mutation Research*, **566**, 231–248.

14. Thon,G., Maki,T., Haber,J.E. and Iwasaki,H. (2019) Mating-type switching by homology-directed recombinational repair: a matter of choice. *Curr Genet*, **65**, 351–362.

15. Bressan,D.A., Vazquez,J. and Haber,J.E. (2004) Mating type–dependent constraints on the mobility of the left arm of yeast chromosome III. *J Cell Biol*, **164**, 361–371.

16. Houston,P.L. and Broach,J.R. (2006) The Dynamics of Homologous Pairing during Mating Type Interconversion in Budding Yeast. *PLOS Genetics*, **2**, e98.

17. Lassadi,I., Kamgoué,A., Goiffon,I., Tanguy-le-Gac,N. and Bystricky,K. (2015) Differential Chromosome Conformations as Hallmarks of Cellular Identity Revealed by Mathematical Polymer Modeling. *PLOS Computational Biology*, **11**, e1004306.

18. Lee,C.-S. and Haber,J.E. (2015) Mating-type Gene Switching in Saccharomyces cerevisiae. In *Mobile DNA III*. John Wiley & Sons, Ltd, pp. 491–514.

19. Finn,E.H., Pegoraro,G., Brandão,H.B., Valton,A.-L., Oomen,M.E., Dekker,J., Mirny,L. and Misteli,T. (2019) Extensive Heterogeneity and Intrinsic Variation in Spatial Genome Organization. *Cell*, **176**, 1502-1515.e10.

20. Haber,J.E. (2002) Uses and abuses of HO endonuclease. In Guthrie,C., Fink,G.R. (eds), *Methods in Enzymology*, Guide to Yeast Genetics and Molecular and Cell Biology - Part B. Academic Press, Vol. 350, pp. 141–164.

21. Connolly,B., White,C.I. and Haber,J.E. (1988) Physical Monitoring of Mating Type Switching in Saccharomyces cerevisiae. *Molecular and Cellular Biology*, **8**, 2342–2349.

22. Xie,Z.-X., Mitchell,L.A., Liu,H.-M., Li,B.-Z., Liu,D., Agmon,N., Wu,Y., Li,X., Zhou,X., Li,B., *et al.* (2018) Rapid and Efficient CRISPR/Cas9-Based Mating-Type Switching of Saccharomyces cerevisiae. *G3 (Bethesda)*, **8**, 173–183.

23. Bystricky,K. (2015) Chromosome dynamics and folding in eukaryotes: Insights from live cell microscopy. *FEBS Letters*, **589**, 3014–3022.

24. Saad,H., Gallardo,F., Dalvai,M., Tanguy-le-Gac,N., Lane,D. and Bystricky,K. (2014) DNA dynamics during early double-strand break processing revealed by non-intrusive imaging of living cells. *PLoS Genet*, **10**, e1004187.

25. Lisby,M., Rothstein,R. and Mortensen,U.H. (2001) Rad52 forms DNA repair and recombination centers during S phase. *Proceedings of the National Academy of Sciences*, **98**, 8276–8282.

26. Robinett,C.C., Straight,A., Li,G., Willhelm,C., Sudlow,G., Murray,A. and Belmont,A.S. (1996) In vivo localization of DNA sequences and visualization of large-scale chromatin organization using lac operator/repressor recognition. *J Cell Biol*, **135**, 1685–1700.

27. Michaelis,C., Ciosk,R. and Nasmyth,K. (1997) Cohesins: chromosomal proteins that prevent premature separation of sister chromatids. *Cell*, **91**, 35–45.

28. Avşaroğlu,B., Bronk,G., Li,K., Haber,J.E. and Kondev,J. (2016) Chromosome-refolding model of mating-type switching in yeast. *Proceedings of the National Academy of Sciences*, **113**, E6929–E6938.

29. Peng,B., Wood,R.J., Nielsen,L.K. and Vickers,C.E. (2018) An Expanded Heterologous GAL Promoter Collection for Diauxie-Inducible Expression in Saccharomyces cerevisiae. *ACS Synth. Biol.*, **7**, 748–751.

30. Tang,H., Wu,Y., Deng,J., Chen,N., Zheng,Z., Wei,Y., Luo,X. and Keasling,J.D. (2020) Promoter Architecture and Promoter Engineering in Saccharomyces cerevisiae. *Metabolites*, **10**, 320.

31. Wu,X. and Haber,J.E. (1995) MATa donor preference in yeast mating-type switching: activation of a large chromosomal region for recombination. *Genes Dev.*, **9**, 1922–1932.

32. Hicks,W.M., Yamaguchi,M. and Haber,J.E. (2011) Real-time analysis of double-strand DNA break repair by homologous recombination. *Proceedings of the National Academy of Sciences*, **108**, 3108–3115.

33. Aylon,Y., Liefshitz,B. and Kupiec,M. (2004) The CDK regulates repair of double-strand breaks by homologous recombination during the cell cycle. *The EMBO Journal*, **23**, 4868–4875.

34. Hossain,Md.A., Lin,Y. and Yan,S. (2018) Single-Strand Break End Resection in Genome Integrity: Mechanism and Regulation by APE2. *Int J Mol Sci*, **19**, 2389.

35. Lyndaker,A.M., Goldfarb,T. and Alani,E. (2008) Mutants Defective in Rad1-Rad10-Slx4 Exhibit a Unique Pattern of Viability During Mating-Type Switching in Saccharomyces cerevisiae. *Genetics*, **179**, 1807–1821.

36. Herskowitz,I. and Jensen,R.E. (1991) [8] Putting the *HO* gene to work: Practical uses for mating-type switching. In *Methods in Enzymology*, Guide to Yeast Genetics and Molecular Biology. Academic Press, Vol. 194, pp. 132–146.

37. Ray,B.L., White,C.I. and Haber,J.E. (1991) Heteroduplex formation and mismatch repair of the 'stuck' mutation during mating-type switching in Saccharomyces cerevisiae. *Mol Cell Biol*, **11**, 5372–5380.

38. Corre,G., Stockholm,D., Arnaud,O., Kaneko,G., Viñuelas,J., Yamagata,Y., Neildez-Nguyen,T.M.A., Kupiec,J.-J., Beslon,G., Gandrillon,O., *et al.* (2014) Stochastic Fluctuations and Distributed Control of Gene Expression Impact Cellular Memory. *PLOS ONE*, **9**, e115574.

39. Goedhart,J., van Weeren,L., Hink,M.A., Vischer,N.O.E., Jalink,K. and Gadella,T.W.J. (2010) Bright cyan fluorescent protein variants identified by fluorescence lifetime screening. *Nat Methods*, **7**, 137–139.

40. Hansen,A.S., Hao,N. and O'Shea,E.K. (2015) High-throughput microfluidics to control and measure signaling dynamics in single yeast cells. *Nat Protoc*, **10**, 1181–1197.

41. Backlund,M.P., Joyner,R., Weis,K. and Moerner,W.E. (2014) Correlations of three-dimensional motion of chromosomal loci in yeast revealed by the double-helix point spread function microscope. *Mol Biol Cell*, **25**, 3619–3629.

42. Shechtman,Y., Gustavsson,A.-K., Petrov,P.N., Dultz,E., Lee,M.Y., Weis,K. and Moerner,W.E. (2017) Observation of live chromatin dynamics in cells via 3D localization microscopy using Tetrapod point spread functions. *Biomed. Opt. Express, BOE*, **8**, 5735–5748.

43. Weiss,L.E., Shalev Ezra,Y., Goldberg,S., Ferdman,B., Adir,O., Schroeder,A., Alalouf,O. and Shechtman,Y. (2020) Three-dimensional localization microscopy in live flowing cells. *Nat. Nanotechnol.*, **15**, 500–506.

44. Finn,E.H., Pegoraro,G., Shachar,S. and Misteli,T. (2017) Comparative analysis of 2D and 3D distance measurements to study spatial genome organization. *Methods*, **123**, 47–55.

45. Jorgensen,P., Edgington,N.P., Schneider,B.L., Rupeš,I., Tyers,M. and Futcher,B. (2007) The Size of the Nucleus Increases as Yeast Cells Grow. *Mol Biol Cell*, **18**, 3523–3532.

46. Belton,J.-M., Lajoie,B.R., Audibert,S., Cantaloube,S., Lassadi,I., Goiffon,I., Baù,D., Marti-Renom,M.A., Bystricky,K. and Dekker,J. (2015) The conformation of yeast chromosome III is mating type-dependent and controlled by the recombination enhancer. *Cell Rep*, **13**, 1855–1867.

47. Milbredt,S. and Waldminghaus,T. (2017) BiFCROS: A Low-Background Fluorescence Repressor Operator System for Labeling of Genomic Loci. *G3 (Bethesda)*, **7**, 1969–1977.

48. Weiss,L.E., Naor,T. and Shechtman,Y. (2018) Observing DNA in live cells. *Biochemical Society Transactions*, **46**, 729–740.

49. Li,J., Coïc,E., Lee,K., Lee,C.-S., Kim,J.-A., Wu,Q. and Haber,J.E. (2012) Regulation of Budding Yeast Mating-Type Switching Donor Preference by the FHA Domain of Fkh1. *PLOS Genetics*, **8**, e1002630.

50. Sun,K., Coïc,E., Zhou,Z., Durrens,P. and Haber,J.E. (2002) Saccharomyces forkhead protein Fkh1 regulates donor preference during mating-type switching through the recombination enhancer. *Genes Dev.*, **16**, 2085–2096.

51. Durocher,D., Henckel,J., Fersht,A.R. and Jackson,S.P. (1999) The FHA Domain Is a Modular Phosphopeptide Recognition Motif. *Molecular Cell*, **4**, 387–394.

52. Wei,L., Nakajima,S., Hsieh,C.-L., Kanno,S., Masutani,M., Levine,A.S., Yasui,A. and Lan,L. (2013) Damage response of XRCC1 at sites of DNA single strand breaks is regulated by phosphorylation and ubiquitylation after degradation of poly(ADP-ribose). *Journal of Cell Science*, **126**, 4414–4423.

53. Loizou,J.I., El-Khamisy,S.F., Zlatanou,A., Moore,D.J., Chan,D.W., Qin,J., Sarno,S., Meggio,F., Pinna,L.A. and Caldecott,K.W. (2004) The Protein Kinase CK2 Facilitates Repair of Chromosomal DNA Single-Strand Breaks. *Cell*, **117**, 17–28.

54. Caldecott,K.W. (2008) Single-strand break repair and genetic disease. *Nat Rev Genet*, **9**, 619–631.

55. Gibson,D.G., Young,L., Chuang,R.-Y., Venter,J.C., Hutchison,C.A. and Smith,H.O. (2009) Enzymatic assembly of DNA molecules up to several hundred kilobases. *Nat Methods*, **6**, 343–345.

56. Nguyen,A.W. and Daugherty,P.S. (2005) Evolutionary optimization of fluorescent proteins for intracellular FRET. *Nat Biotechnol*, **23**, 355–360.

57. Lee,M.E., DeLoache,W.C., Cervantes,B. and Dueber,J.E. (2015) A Highly Characterized Yeast Toolkit for Modular, Multipart Assembly. *ACS Synth Biol*, **4**, 975–986.

58. Li,D., Song,J.-Z., Shan,M.-H., Li,S.-P., Liu,W., Li,H., Zhu,J., Wang,Y., Lin,J. and Xie,Z. (2015) A fluorescent tool set for yeast Atg proteins. *Autophagy*, **11**, 954–960.

59. Day,K.J., Casler,J.C. and Glick,B.S. (2018) Budding Yeast Has a Minimal Endomembrane System. *Dev Cell*, **44**, 56-72.e4.

60. Baker Brachmann,C., Davies,A., Cost,G.J., Caputo,E., Li,J., Hieter,P. and Boeke,J.D. (1998) Designer deletion strains derived from Saccharomyces cerevisiae S288C: A useful set of strains and plasmids for PCR-mediated gene disruption and other applications. *Yeast*, **14**, 115–132.

61. Gietz,R.D. and Schiestl,R.H. (2007) High-efficiency yeast transformation using the LiAc/SS carrier DNA/PEG method. *Nat Protoc*, **2**, 31–34.

62. Amino Acid Mix (10×) (2016) *Cold Spring Harbor Protocols*, **2016**, pdb.rec090308.

63. Pfaffl,M.W. (2001) A new mathematical model for relative quantification in real-time RT-PCR. *Nucleic Acids Res*, **29**, e45.

64. Ayala-Torres,S., Chen,Y., Svoboda,T., Rosenblatt,J. and Van Houten,B. (2000) Analysis of Gene-Specific DNA Damage and Repair Using Quantitative Polymerase Chain Reaction. *Methods*, **22**, 135–147.

65. Saguy,A. (2024) alonsaguy/DNA-double-strand-break-repair-quantification-and-tracking.

66. Schmidt,U., Weigert,M., Broaddus,C. and Myers,G. (2018) Cell Detection with Star-Convex Polygons. In Frangi,A.F., Schnabel,J.A., Davatzikos,C., Alberola-López,C., Fichtinger,G. (eds), *Medical Image Computing and Computer Assisted Intervention – MICCAI 2018*. Springer International Publishing, Cham, pp. 265–273.

## VIDEOS

**Movie S1 -** Tracking switching-induced, surface-adhered single cells in a microfluidic channel over time enables the detection of switched cells (CFP expression), mating between opposite types, and diploid cell budding.